

# Current-induced switching in a magnetic insulator

Can Onur Avci, Andy Quindeau, Chi-Feng Pai<sup>†</sup>, Maxwell Mann, Lucas Caretta, Astera S. Tang, Mehmet C. Onbasli, Caroline A. Ross<sup>\*</sup> and Geoffrey S. D. Beach<sup>\*</sup>

**The spin Hall effect in heavy metals converts charge current into pure spin current, which can be injected into an adjacent ferromagnet to exert a torque. This spin-orbit torque (SOT) has been widely used to manipulate the magnetization in metallic ferromagnets. In the case of magnetic insulators (MIs), although charge currents cannot flow, spin currents can propagate, but current-induced control of the magnetization in a MI has so far remained elusive. Here we demonstrate spin-current-induced switching of a perpendicularly magnetized thulium iron garnet film driven by charge current in a Pt overlayer. We estimate a relatively large spin-mixing conductance and damping-like SOT through spin Hall magnetoresistance and harmonic Hall measurements, respectively, indicating considerable spin transparency at the Pt/MI interface. We show that spin currents injected across this interface lead to deterministic magnetization reversal at low current densities, paving the road towards ultralow-dissipation spintronic devices based on MIs.**

Ferromagnetic thin-film heterostructures provide the basis for hard disk data storage, magnetic random access memory, magnetic sensor technology based on giant- and tunnel magnetoresistance, and, more recently, prototypes of logic and memory using domain walls. The ability to manipulate the magnetic state of thin-film heterostructures is an essential attribute of these devices, and it is especially attractive if it can be accomplished electrically, rather than by the application of a magnetic field. Compared to conventional spin transfer torque effects demonstrated in spin-valves and magnetic tunnel junctions, the current-induced spin-orbit torque (SOT) in non-magnetic heavy metal/metallic ferromagnet heterostructures<sup>1,2</sup> and magnetically doped topological insulator heterostructures at low temperatures<sup>3,4</sup> provides a highly efficient way to control the magnetization of the ferromagnetic material. With the SOT mechanism it is possible to realize magnetization switching<sup>5,6</sup>, magnetic oscillations<sup>7,8</sup>, and ultrafast chiral domain wall motion<sup>9,10</sup>. Spin currents generated by the spin Hall effect (SHE)<sup>11</sup> in heavy metals (HM) have been shown to be a dominant source of the damping-like SOT responsible for the observed switching and domain wall motion in such heterostructures.

In the case of magnetic insulators (MIs) such as yttrium iron garnet (YIG), charge currents cannot flow, but spin currents generated by the SHE in an adjacent HM layer can be transmitted across the HM/MI interface. This has been shown to give rise to novel spin transport phenomena such as spin Hall magnetoresistance (SMR) in HM/MI structures<sup>12–15</sup>, and used to excite high-frequency magnetization dynamics in YIG<sup>16,17</sup> driven by current-induced spin torques. The low damping and long spin transmission length ( $\sim 1$  mm) in magnetic insulators such as YIG make them promising candidates for spin-wave communication and ultralow-power-dissipation applications<sup>16,18</sup>, as well as insulating components of magnetic logic or memory devices. However, SHE-induced control of the magnetization switching in a magnetic insulator has yet to be reported.

In this work, we demonstrate deterministic current-induced switching in a perpendicularly magnetized MI using spin torque from the SHE in an adjacent Pt layer. The MI used here consists

of an 8-nm-thick thulium iron garnet ( $\text{Tm}_3\text{Fe}_5\text{O}_{12}$ , TmIG) film with perpendicular magnetic anisotropy. We organize this article as follows: first, we report on the structural and magnetic characterization of TmIG continuous films with X-ray diffraction (XRD), vibrating sample magnetometry (VSM), magneto-optical Kerr effect (MOKE) and magnetic force microscopy (MFM). Next, we characterize SMR by means of transverse (Hall effect) measurements in TmIG/Pt bilayers, from which we extract the spin-mixing conductance  $G^{\uparrow\downarrow}$  that characterizes spin transport across the interface. Then, we perform harmonic Hall effect measurements to accurately quantify the damping-like SOT driven by the spin Hall effect in Pt. Finally, we show that the perpendicular magnetization of TmIG can be reversed by the damping-like SOT stemming from the SHE in an adjacent Pt layer with current densities comparable to or lower than that used to switch all-metallic perpendicular magnetic anisotropy (PMA) heterostructures<sup>5,6</sup>, even though the magnetic film thickness is one order of magnitude larger. These results are an important step towards novel memory or logic devices based on MIs.

## Structural and magnetic characterization

Ferrimagnetic TmIG was chosen because its negative magnetostriction and negative magnetocrystalline anisotropy coefficient  $K_1$  leads to an out-of-plane easy axis<sup>19</sup> when grown epitaxially under tensile strain on a (111)-oriented gadolinium gallium garnet ( $\text{Gd}_3\text{Ga}_5\text{O}_{12}$ , GGG) substrate. Films with layer thicknesses of 8 nm and 30 nm TmIG were grown by pulsed laser deposition (PLD) on GGG (111). The 8 nm film was used in the SOT switching experiments, whereas the 30 nm film yields a stronger signal for XRD analysis that gives insight into the structure and strain state of TmIG. The crystalline structure and film thickness were investigated by high-resolution XRD and X-ray reflectivity (XRR), respectively. For the 30-nm-thick film the symmetric XRD scans around the (444) GGG-substrate and TmIG peaks (Fig. 1a) demonstrate fully strained TmIG films with the anticipated Laue diffraction peak shape and Laue fringes. Reciprocal space mapping of the 30 nm TmIG film provides evidence that the in-plane lattice parameter of TmIG was coherently strained to match that of GGG (111) (see Supplementary Information 1). High-resolution

Department of Materials Science and Engineering, Massachusetts Institute of Technology, Cambridge, Massachusetts 02139, USA. <sup>†</sup>Present address: Department of Materials Science and Engineering, National Taiwan University, Taipei 10617, Taiwan. \*e-mail: [caross@mit.edu](mailto:caross@mit.edu); [gbeach@mit.edu](mailto:gbeach@mit.edu)

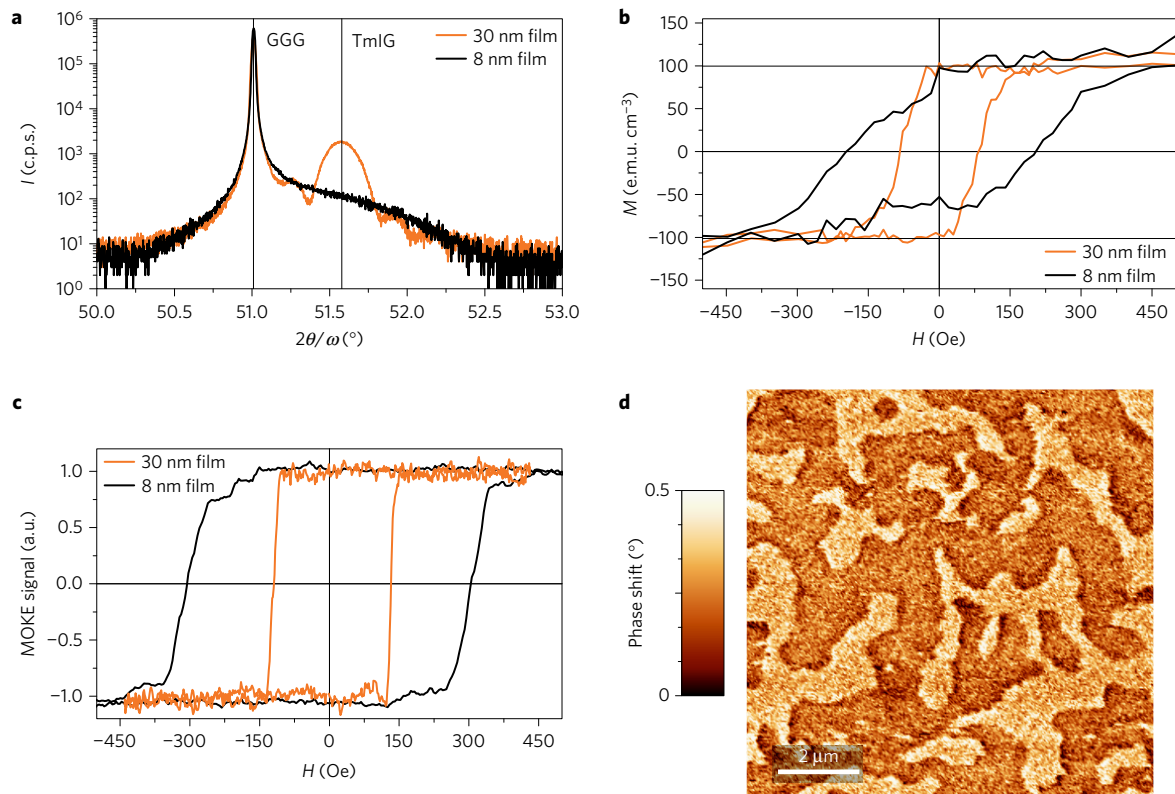


**Figure 1 | Structural and magnetic properties of PMA TmIG.** **a**, X-ray diffraction patterns ( $2\theta - \omega$  scan) of a 30-nm-thick (orange) and a 8-nm-thick (black) TmIG film grown on (111)-oriented GGG substrates. **b**, Magnetization of both films as a function of out-of-plane magnetic field  $H_z$  obtained by VSM. A paramagnetic contribution from the GGG substrate has been subtracted. **c**, Polar MOKE signal of films. **d**, MFM image of the as-grown 30-nm-thick TmIG film showing up- and down-oriented domains as regions of light and dark contrast.

transmission electron microscopy of a similar film (not shown here) revealed a fully coherent interface with no dislocations over at least a  $1.5 \mu\text{m}$  distance. Since the thicker TmIG film showed no strain relaxation, it is reasonable to assume that the thinner (8 nm) TmIG film is also fully coherent.

Figure 1b,c shows the out-of-plane hysteresis loop for the 8 nm and 30 nm TmIG films measured using VSM and polar MOKE, respectively. Both films exhibit high out-of-plane remanence, indicating strong PMA. The coercivity of the 30 nm film is lower than that of the 8 nm film. We tentatively attribute this behaviour to the difference in the domain size, which is expected to be proportional to the square root of thickness, leading to the thickness dependence of the field needed to nucleate and propagate domains. The saturation magnetization of both films was about  $100 \text{ e.m.u. cm}^{-3}$ , approaching the room-temperature bulk value<sup>20</sup> of  $M_s \sim 110 \text{ e.m.u. cm}^{-3}$ . The magnetic domain configuration was visualized in both the as-grown (demagnetized) and saturated states via magnetic force microscopy (MFM). Figure 1d shows an MFM image for the demagnetized state in the 30 nm film, which exhibits a labyrinthine domain structure typical of PMA thin films. After out-of-plane saturation, the domain structure vanishes (not shown), consistent with the high remanence of the corresponding hysteresis loops.

### Spin Hall magnetoresistance

SMR measurements have been widely used to extract spin transport parameters in transition HM/MI bilayers<sup>12–15</sup>, from which the interfacial spin-mixing conductance  $G^{\uparrow\downarrow}$  can be estimated. In such measurements, an electrical current is applied to a HM layer with sizeable SHE deposited on a MI. The charge current  $\mathbf{j}$  in the HM generates a transverse spin current  $\mathbf{j}_s = \theta_{\text{SH}}(\mathbf{j} \times \boldsymbol{\sigma})$  that will either be transmitted or reflected at the HM/MI interface depending on the

relative orientations between the SHE spin polarization  $\boldsymbol{\sigma}$  and the magnetization direction  $\mathbf{m}$  in the MI. Here  $\theta_{\text{SH}}$  represents the spin Hall angle (SHA) of the HM. Interfacial spin transmission/reflection is characterized by the spin-mixing conductance  $G^{\uparrow\downarrow} = G_r^{\uparrow\downarrow} + iG_i^{\uparrow\downarrow}$ . The real part  $G_r^{\uparrow\downarrow}$  is related to the damping-like torque acting upon  $\mathbf{m}$ , which is proportional to  $\mathbf{m} \times (\boldsymbol{\sigma} \times \mathbf{m})$ . The imaginary part  $G_i^{\uparrow\downarrow}$  is associated with a field-like torque, which is proportional to  $\boldsymbol{\sigma} \times \mathbf{m}$ . The dependence of spin transmission/reflection on  $\mathbf{m}$  and  $\boldsymbol{\sigma}$  will further modulate  $\mathbf{j}$  in the HM layer due to the inverse spin Hall effect<sup>21</sup>. This leads to magnetoresistance in the HM, the so-called SMR, which possesses a symmetry distinct from that of, for example, anisotropic magnetoresistance.

In the SMR scenario, the longitudinal ( $R$ ) and transverse Hall ( $R_H$ ) resistance in a HM/MI bilayer can be expressed as<sup>13,15,22</sup>

$$R = R_0 + \Delta R^{\text{SMR}} \sin^2 \theta \sin^2 \varphi \quad (1)$$

$$R_H = R_H^{\text{SMR}} \sin^2 \theta \sin 2\varphi + R_H^{\text{AHE,SMR}} \cos \theta + R_H^{\text{OHE}} H_z \quad (2)$$

where  $R_0$  and  $\Delta R^{\text{SMR}}$  represent the  $\mathbf{m}$ -independent longitudinal resistance and the modulation due to the SMR, respectively.  $R_H^{\text{SMR}}$ ,  $R_H^{\text{AHE,SMR}}$  and  $R_H^{\text{OHE}}$  represent the transverse manifestation of SMR, the SMR-induced anomalous Hall effect (AHE) resistance, and the ordinary Hall resistance of the HM, respectively. The magnetization angles  $\theta$ ,  $\varphi$  are defined in Fig. 2a, as well as the coordinate system used throughout the article. We note that the transverse SMR and the SMR-induced AHE are identical to the planar Hall resistance and anomalous Hall resistance in conducting ferromagnets by symmetry.

Figure 2b–d summarizes measurements of transverse resistance  $R_H$  on TmIG(8 nm)/Pt(5 nm) bilayers that reveal SMR in our films

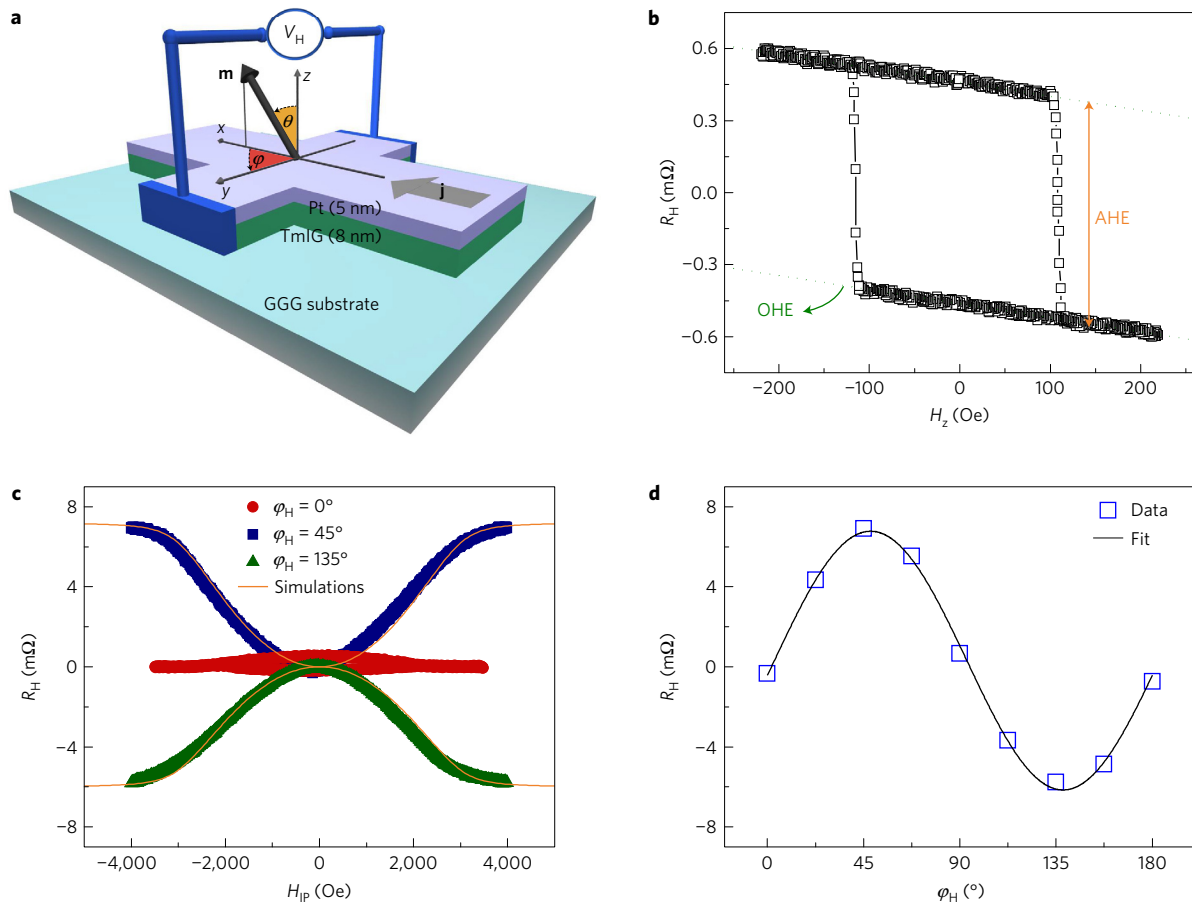


**Figure 2 | SMR measurements on a TmIG/Pt bilayer device.** **a**, Hall device schematics, coordinate systems and the electrical measurement set-up. **b**, Hall resistance  $R_H$  is measured with an out-of-plane field  $H_z$  and an a.c. current of amplitude 1.5 mA (r.m.s.), corresponding to  $j = 4.3 \times 10^{10}$  A m $^{-2}$  in the Pt layer.  $R_H$  tracks the magnetization vector, due to the SMR-induced AHE, which switches between up and down states at the coercive field of  $H_c = 110 \pm 5$  Oe. The linear negative slope arises from the ordinary Hall effect, scaling linearly with  $H_z$  and independent of the magnetization direction. **c**,  $R_H$  measured while sweeping an in-plane field ( $H_{IP}$ ) at  $\varphi_H = 0^\circ, 45^\circ, 135^\circ$  in the presence of a constant  $H_z = +200$  Oe to ensure that the magnetization remains single domain during measurement. The curves at  $\varphi_H = 45^\circ (135^\circ)$  are representative of SMR behaviour where a large positive (negative) signal appears when  $\mathbf{m}$  is saturated in-plane. Orange curves are simulations based on experimental parameters and an estimated perpendicular magnetic anisotropy field  $H_K = 2,700$  Oe. **d**, Summary of  $R_H$  measurements performed at different  $\varphi_H$  as shown in **c**. A fit to the data according to equation (2) reveals  $R_H^{\text{SMR}} = 6.5$  m $\Omega$ . Note that a constant sample-dependent offset is subtracted from the raw data shown in **b** and **c**.

and allow the associated transport parameters to be quantified (see Supplementary Information 2 for the longitudinal SMR measurements). The bilayer was patterned into Hall cross devices, as shown schematically in Fig. 2a, and all electrical measurements were performed using a standard lock-in technique (see Methods).  $R_H$  versus  $H_z$  (Fig. 2b) shows 100% remanence and sharp magnetization reversal at a coercive field  $H_c = 110 \pm 5$  Oe. We attribute the reduction in  $H_c$  as compared to the continuous film (Fig. 1) to geometrical effects due to patterning. The linear background (green dotted line) arises from the ordinary Hall effect in Pt, consistent with equation (2). We find  $R_H^{\text{AHE,SMR}} = -0.46$  m $\Omega$  and  $R_H^{\text{OHE}} = -5.8$  m $\Omega$  T $^{-1}$ , which yield  $\rho_{xy}^{\text{AHE,SMR}} = -2.3 \times 10^{-4}$   $\mu\Omega$  cm and  $\rho_{xy}^{\text{OHE}} = -2.9 \times 10^{-3}$   $\mu\Omega$  cm T $^{-1}$ , respectively, comparable to recently reported values in Pt/YIG<sup>22</sup>. Next, we measure  $R_H$  as a function of in-plane field ( $H_{IP}$ ) at different field angles  $\varphi_H$ . Figure 2c shows measurements recorded at  $\varphi_H = 0^\circ, 45^\circ$  and  $135^\circ$ , where the SMR contribution to  $R_H$  is either zero at  $\varphi_H = 0^\circ$  or maximum (minimum) at  $\varphi_H = 45^\circ (135^\circ)$  according to equation (2). Note that we have applied a fixed out-of-plane field  $H_{OOP} = 200$  Oe during the  $H_{IP}$  sweep to avoid magnetic domain formation and to ensure coherent rotation of the magnetization. By simulating the SMR with a macrospin model using experimental parameters (Fig. 2c, orange curves) we obtain a perpendicular magnetic anisotropy field

$H_K \approx 2,700$  Oe. Finally, by repeating the measurements at various  $\varphi_H$  we find that  $R_H \propto \sin 2\varphi$ , as shown in Fig. 2d, as expected from the SMR. A fit to the data yields  $R_H^{\text{SMR}} = 6.5$  m $\Omega$ , which leads to  $\rho_{xy}^{\text{SMR}} = 3.25 \times 10^{-3}$   $\mu\Omega$  cm. This value is approximately 14 times larger than the SMR-induced AHE, implying that the real part of the spin-mixing conductance is significantly larger than the imaginary part.

Following the SMR model given in ref. 23 and by using  $\rho_{xx}^{\text{SMR}}, \rho_{xy}^{\text{AHE,SMR}}$  obtained above, we can calculate  $G_r^{\uparrow\downarrow}$ . By taking  $\rho_{xx}^{\text{Pt}} = 40.4$   $\mu\Omega$  cm as measured on the same device, assuming  $\theta_{\text{SH}} = 0.08$  for Pt<sup>24</sup> and taking the spin diffusion length to be  $\lambda_{\text{Pt}} = 1.4$  nm (ref. 23), we estimate  $G_r^{\uparrow\downarrow} = 1.0 \times 10^{14}$   $\Omega^{-1}$  m $^{-2}$  and  $G_i^{\uparrow\downarrow} = 7.1 \times 10^{12}$   $\Omega^{-1}$  m $^{-2}$ , which compare well with commonly accepted values for YIG/Pt<sup>13,14</sup>.

### Determination of damping-like spin-orbit torque

The large  $G_r^{\uparrow\downarrow}$  suggests the possibility of achieving significant spin injection across the TmIG/Pt interface, and hence exerting a damping-like torque on the magnetization. To quantify the SHE-induced SOT, we performed harmonic Hall effect measurements similar to those commonly used in all-metallic HM/ferromagnet bilayers<sup>1,25</sup>. In such measurements, an a.c. current induces oscillations in the magnetization due to alternating SOT, giving rise

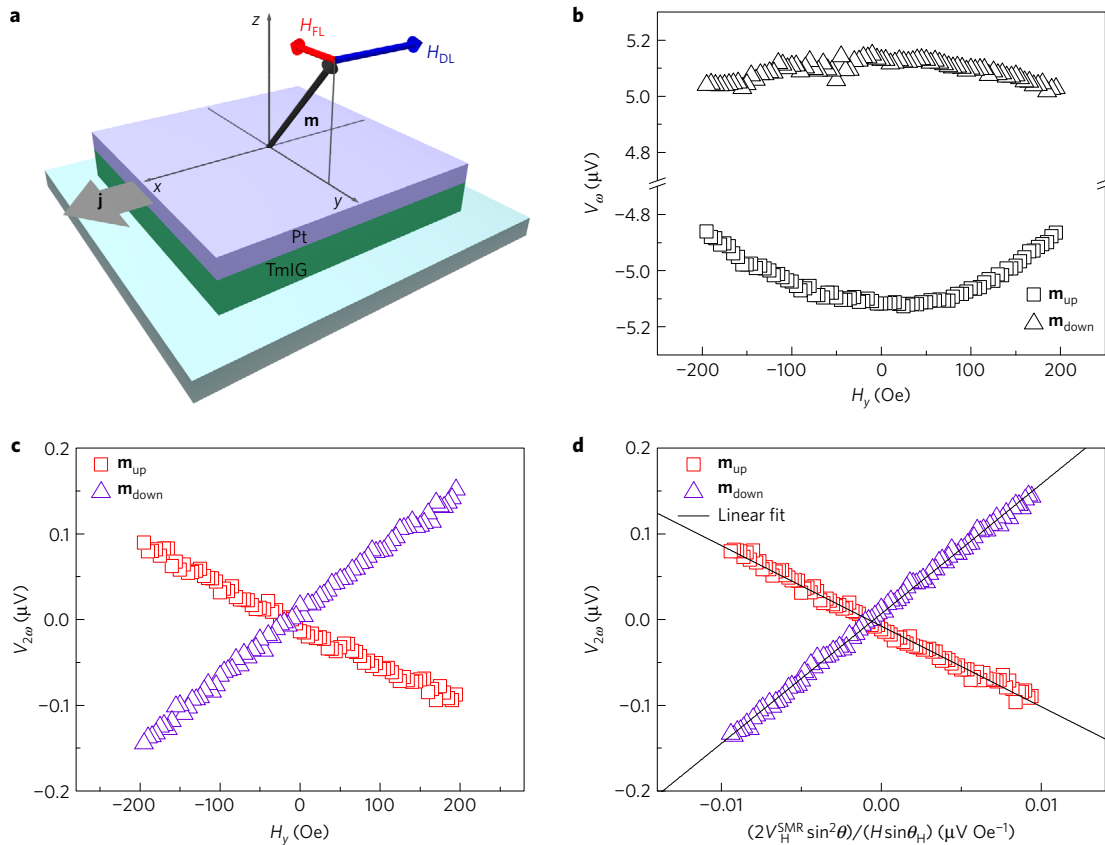


**Figure 3 | Determination of the damping-like SOT in TmIG/Pt by harmonic measurements.** **a**, Measurement geometry for the harmonic Hall voltage measurements. Blue and red arrows show the effective fields associated with damping-like ( $H_{DL}$ ) and field-like ( $H_{FL}$ ) SOT, respectively, for current flow along the  $x$ -axis and magnetization tilted along the  $y$ -axis. **b**, First-harmonic Hall voltage ( $V_{\omega}$ ) mainly driven by the SMR-induced AHE, acquired during an in-plane field sweep of  $H_y = \pm 200$  Oe with an applied current of  $j_{r.m.s.} = 2.1 \times 10^{11}$  A m $^{-2}$ . The curvature is different for  $\mathbf{m}_{up}$  and  $\mathbf{m}_{down}$  due to misalignment of the external field with respect to the  $y$ -axis, causing a small SMR contribution which is even with respect to magnetization reversal whereas SMR-induced AHE is odd. **c**, Second-harmonic voltage ( $V_{2\omega}$ ) recorded under the same conditions as in **b**. Different slopes are a consequence of a current-induced spin Seebeck effect voltage (see text and Supplementary Information 4 and 5 for more details). **d**,  $V_{2\omega}$  plotted versus  $(2V_H^{SMR} \sin^2 \theta)/(H \sin \theta_H)$  to quantify  $H_{DL}$  by evaluating the slope given by the linear fit (black curves). A constant sample-dependent offset has been subtracted from the data presented in **b** and **c**.

to a second-harmonic Hall voltage,  $V_{2\omega}$ . Usually, the damping-like and field-like torques are probed by measuring  $V_{2\omega}$  while sweeping an in-plane magnetic field that tilts the magnetization in the  $zx$  and  $zy$  planes, respectively. Under these conditions the a.c. current generates out-of-plane magnetization oscillations in the respective planes, and the resulting AHE oscillations dominate the  $V_{2\omega}$  signal. In the present system, however, the SMR is much larger than the SMR-induced AHE, and hence  $V_{2\omega}$  mainly reflects the in-plane component of magnetization oscillations. In this case, the damping-like SOT is expected to give the dominant contribution to  $V_{2\omega}$  when the magnetization is tilted in the  $zy$  plane, since the field-like torque drives out-of-plane oscillations, whose contribution to  $V_{2\omega}$  scales with the much smaller SMR-induced AHE. At the same time, thermal contributions to  $V_{2\omega}$  from the spin Seebeck effect (SSE) arising from the Joule-heating-induced perpendicular temperature gradient scale as  $V_{SSE} \propto \nabla T_z \times \mathbf{m}$ , and are hence minimized in this configuration<sup>26</sup>. Therefore, harmonic Hall measurements under a transverse field are well-suited to quantitatively extract the damping-like SOT in this system.

Figure 3b and c shows the first- and second-harmonic signals when  $\mathbf{m}$  is tilted along  $\pm y$  with a swept field  $H_y$  and an a.c. current density  $j_{r.m.s.} \cong 2.1 \times 10^{11}$  A m $^{-2}$ . Ideally, the first-harmonic signal  $V_{\omega}$  arises solely from the SMR-induced AHE in this geometry (see equation (2)), which decreases with increasing  $H_y$  as  $\mathbf{m}$  tilts towards the plane ( $V_{\omega} = V_H^{AHE,SMR} \cos \theta$ ). However, unintentional misalignment of  $H$  with respect to the  $y$  axis creates non-negligible

SMR ( $\propto \sin^2 \theta$ ) and OHE ( $\propto H_z$ ) contributions that distort the expected quadratic AHE signal, as depicted in Fig. 3b.

We now focus on  $V_{2\omega}$  which, as shown in Fig. 3c, varies linearly with  $H_y$ , having opposite slopes for up ( $\mathbf{m}_{up}$ ) and down ( $\mathbf{m}_{down}$ ) magnetization states. This symmetry is typical for a SOT signal and can be driven by both  $H_{FL}$  and  $H_{DL}$  according to ref. 1:

$$V_{2\omega}^{\varphi=90^\circ} = (V_H^{AHE,SMR} - 2V_H^{SMR} \cos \theta \sin 2\varphi) \frac{d \cos \theta}{dH} \frac{H_{FL}}{\sin(\theta_H - \theta)} + 2V_H^{SMR} \sin^2 \theta \cos 2\varphi \frac{H_{DL}}{H \sin \theta_H} \quad (3)$$

where  $\theta_H$  is the out-of-plane angle of the external field. Since  $V_H^{SMR} \gg V_H^{AHE,SMR}$ , and assuming  $H_{DL} \approx H_{FL}$ , the signal in Fig. 3c must be dominated by the second term on the right-hand side. Therefore, to estimate the damping-like SOT we plot  $V_{2\omega}$  as a function of  $(2V_H^{SMR} \sin^2 \theta)/(H \sin \theta_H)$  in Fig. 3d (note that  $\cos 2\varphi \cong \sin \theta_H \cong 1$  and  $\sin 2\varphi \cong 0$  when  $H_y$  tilts the sample magnetization in the  $zy$  plane) and take the slope, which directly yields  $H_{DL}$  in units of Oe. We obtain  $-9.4$  Oe and  $+15.1$  Oe for  $\mathbf{m}_{up}$  and  $\mathbf{m}_{down}$ , respectively, giving on average  $H_{DL} = 12.3 \pm 2.8$  Oe per  $j_{r.m.s.} \cong 2.1 \times 10^{11}$  A m $^{-2}$ , with the sign compatible with the SHE in Pt. The difference in slopes between  $\mathbf{m}_{up}$  and  $\mathbf{m}_{down}$  is due to a small  $x$ -component creating a non-negligible  $V_{SSE}$ , adding a positive slope for both up and down orientation (see Supplementary

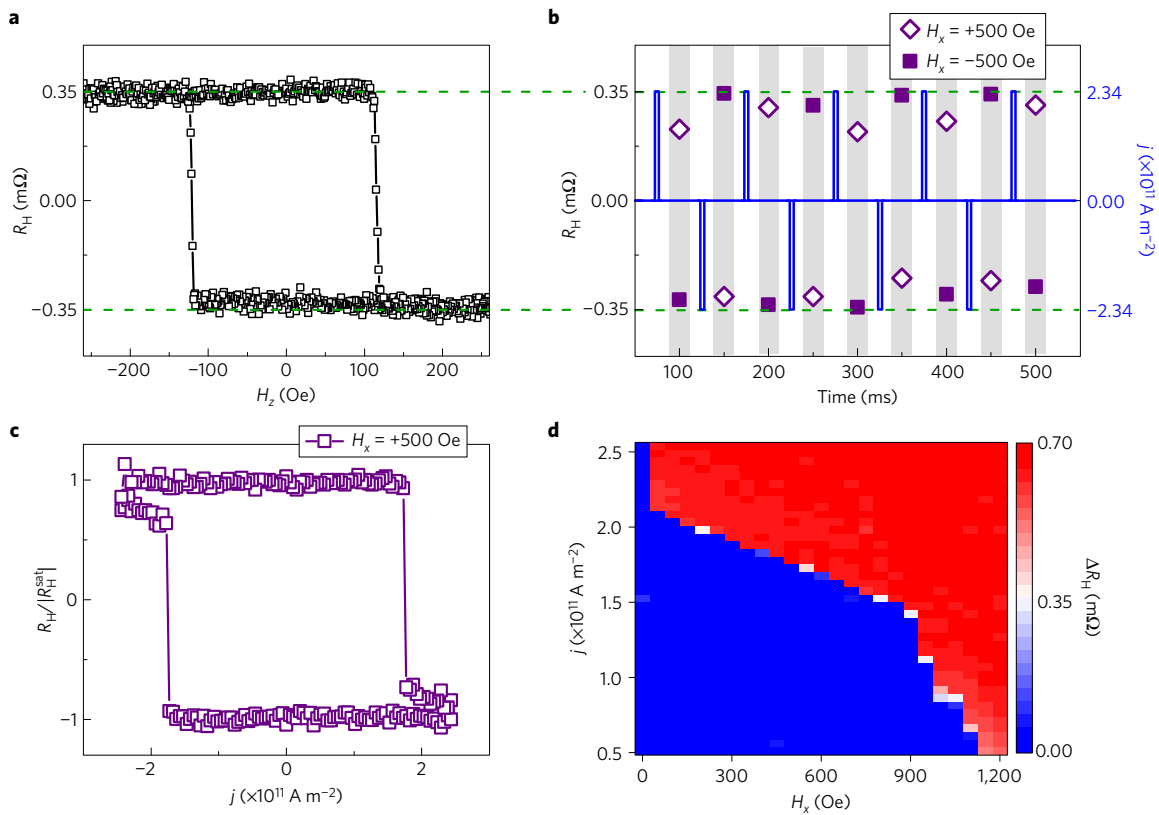


**Figure 4 | Current-induced magnetization switching of TmIG/Pt.** **a**, Hall resistance measurements serving as reference for  $\mathbf{m}_{\text{up}}$  and  $\mathbf{m}_{\text{down}}$  states (a constant offset and planar Hall effect (PHE) contribution are subtracted). **b**, Magnetization switching with 5-ms-long current pulses of  $j = \pm 2.34 \times 10^{11} \text{ A m}^{-2}$  amplitude in the presence of an external field of  $H_x = \pm 500 \text{ Oe}$ . The switching polarity changes on reversing either the current polarity or field direction. **c**, Switching behaviour of the device as a function of the injected current density for a given field of  $H_x = +500 \text{ Oe}$ . Above the critical current of  $j_c = \pm 1.7 \times 10^{11} \text{ A m}^{-2}$  the magnetization switches systematically and reproducibly. **d**, Magnetization switching phase diagram showing the switching behaviour as a function of applied current and field. It is constructed with the help of measurements shown in **c** performed with  $H_x = 0 \rightarrow 1,200 \text{ Oe}$ .

Information 4). By assuming that  $H_{\text{DL}}$  is entirely driven by the SHE, we can estimate the SHA via<sup>27</sup>  $\theta_{\text{SH}} = (2e/\hbar)(M_s t_{\text{Pt}} H_{\text{DL}}/j)$  using appropriate material parameters, where  $e$  is the elementary charge,  $\hbar$  is the reduced Planck constant,  $M_s$  is the saturation magnetization of TmIG and  $t_{\text{Pt}}$  is the Pt layer thickness. We find  $\theta_{\text{SH}} \approx 1\%$ , which constitutes the lower bound due to current spread to the Hall voltage branches, effectively reducing the current density of the central area of the Hall cross<sup>1,28</sup>. When this correction is taken into account we estimate  $\theta_{\text{SH}} \sim 1.5\text{--}2\%$ , close to the reported values for Pt in contact with YIG<sup>13</sup>.

### Current-induced magnetization switching

Next, we show that the large damping-like SOT revealed by harmonic measurements can be used to switch the magnetization of TmIG, as summarized in Fig. 4. First, we recorded the Hall resistance during a  $H_z$  sweep, as shown in Fig. 4a, from which we subtracted a sample-dependent constant offset and the OHE contribution. This serves as reference for  $\mathbf{m}_{\text{up}}$  and  $\mathbf{m}_{\text{down}}$ , to which we compare the action of the current pulses. We then successively applied  $\pm 5\text{-ms}$ -long pulses of amplitude  $j = 2.34 \times 10^{11} \text{ A m}^{-2}$  in the presence of an in-plane field of  $H_x = \pm 500 \text{ Oe}$  along the current injection axis. We note that for deterministic SOT-induced switching in PMA materials it is necessary to apply an in-plane external field to break the rotational symmetry of  $H_{\text{DL}}$  (ref. 5,6). In Fig. 4b we show the measured Hall resistance after each current pulse in the presence of a constant  $H_x$ . We observe that  $R_H$  changes between 80–100% with respect to its full amplitude—that is, 0.7 mΩ, after every pulse. The switching polarity reverses when reversing

the applied field direction  $+H_x \rightarrow -H_x$ , as expected from the SOT-induced switching. Reference measurements performed with the identical configuration showed that the switching polarity is compatible with that of Pt/Co when the structural inversion factor is taken into account (Supplementary Information 6).

Figure 4c shows the switching behaviour of the same sample as a function of  $j$  for  $H_x = +500 \text{ Oe}$ . Each data point represents the outcome of averaging ten measurement sequences where, during each sequence, we measured  $R_H$  after a given pulse was applied synchronously with  $H_x$ , and compared with the reference  $R_H$  recorded after positive and negative out-of-plane saturation field pulses (for details of the measurement protocol see Supplementary Information 6). We see that the switching events are systematic above the critical current density of  $j_c = 1.8 \times 10^{11} \text{ A m}^{-2}$  for this specific  $H_x$ . We note that the switching events above  $j_c$  saturate around 90%, meaning that the probed area of the Hall cross does not fully reverse. This behaviour was reproducible for several devices and tentatively explained by partial switching of areas in the vicinity of the Hall cross where  $j$  is relatively lower but still contributes to  $R_H$ .

To examine the switching behaviour in more detail, we repeated the measurements shown in Fig. 4c for fields between 0–1,200 Oe, and constructed the switching probability phase diagram shown in Fig. 4d. Red (blue) colour shows where  $\mathbf{m}$  can (cannot) be switched between up and down states with the combined action of  $j$  and  $H_x$ , as determined by averaging ten switching events. We observe several interesting features. First, the minimum  $H_x$  required for switching is as low as several tens of Oe. Second, the switching phase boundary exhibits two regimes above and below  $H_x = 900 \text{ Oe}$ .

We speculate that for  $H_x > 900$  Oe it becomes comparable to an effective decrease of the anisotropy field due to Joule heating, and thus a significant decrease of the energy necessary to switch **m**. On the other hand, for  $H_x < 900$  Oe the behaviour is quasi-linear, similar to the data reported for, for example, Ta/CoFeB<sup>29</sup>. Finally, we find that switching is possible for current densities as low as  $j = 0.5 \times 10^{11}$  A m<sup>-2</sup>, much lower than in all-metallic systems, despite the relatively small  $\theta_{\text{SH}}$  found with harmonic measurements in the single-domain state. Since magnetization reversal is mediated by a domain nucleation and propagation<sup>30</sup>, this behaviour suggests that the damping-like SOT acting on domain walls is far more efficient than in metallic systems. We also note that Joule heating (see Supplementary Information 7) probably reduces the coercivity, which may play a role in reducing the switching current threshold at higher current densities.

In summary, we show highly efficient magnetization switching of an insulating ferrimagnet with PMA utilizing the spin Hall effect of an adjacent Pt layer. Spin Hall magnetoresistance and harmonic measurements show considerable spin-mixing conductance and damping-like torque, explaining the observed behaviour. These results open up a range of possibilities from both fundamental and applied viewpoints. Detection of perpendicular magnetization in an insulator via the anomalous Hall effect with unprecedented precision makes characterization of magnetic domain wall dynamics electrically accessible. Furthermore, the harmonic measurement scheme introduced here makes the SHE characterization of metal/insulating systems feasible and fast. Finally, the deterministic magnetization switching and its detection represent a significant advance towards the development of room-temperature spintronic devices based on magnetic insulators.

## Methods

Methods and any associated references are available in the [online version of the paper](#).

Received 12 April 2016; accepted 12 September 2016;  
published online 21 November 2016

## References

- Garello, K. *et al.* Symmetry and magnitude of spin-orbit torques in ferromagnetic heterostructures. *Nat. Nanotech.* **8**, 587–593 (2013).
- Brataas, A. & Hals, K. M. D. Spin-orbit torques in action. *Nat. Nanotech.* **9**, 86–88 (2014).
- Fan, Y. *et al.* Magnetization switching through giant spin-orbit torque in a magnetically doped topological insulator heterostructure. *Nat. Mater.* **13**, 699–704 (2014).
- Fan, Y. *et al.* Electric-field control of spin-orbit torque in a magnetically doped topological insulator. *Nat. Nanotech.* **11**, 352–360 (2016).
- Miron, I. M. *et al.* Perpendicular switching of a single ferromagnetic layer induced by in-plane current injection. *Nature* **476**, 189–193 (2011).
- Liu, L. Q. *et al.* Spin-torque switching with the giant spin Hall effect of tantalum. *Science* **336**, 555–558 (2012).
- Demidov, V. E. *et al.* Magnetic nano-oscillator driven by pure spin current. *Nat. Mater.* **11**, 1028–1031 (2012).
- Liu, L. Q., Pai, C.-F., Ralph, D. C. & Buhrman, R. A. Magnetic oscillations driven by the spin Hall effect in 3-terminal magnetic tunnel junction devices. *Phys. Rev. Lett.* **109**, 186602 (2012).
- Emori, S., Bauer, U., Ahn, S. M., Martinez, E. & Beach, G. S. D. Current-driven dynamics of chiral ferromagnetic domain walls. *Nat. Mater.* **12**, 611–616 (2013).
- Ryu, K. S., Thomas, L., Yang, S. H. & Parkin, S. Chiral spin torque at magnetic domain walls. *Nat. Nanotech.* **8**, 527–533 (2013).
- Sinova, J., Valenzuela, S. O., Wunderlich, J., Back, C. H. & Jungwirth, T. Spin Hall effects. *Rev. Mod. Phys.* **87**, 1213–1259 (2015).
- Nakayama, H. *et al.* Spin Hall magnetoresistance induced by a nonequilibrium proximity effect. *Phys. Rev. Lett.* **110**, 206601 (2013).
- Hahn, C. *et al.* Comparative measurements of inverse spin Hall effects and magnetoresistance in YIG/Pt and YIG/Ta. *Phys. Rev. B* **87**, 174417 (2013).
- Weiler, M. *et al.* Experimental test of the spin mixing interface conductivity concept. *Phys. Rev. Lett.* **111**, 176601 (2013).
- Vlietstra, N., Shan, J., Castel, V., van Wees, B. J. & Ben Youssef, J. Spin-Hall magnetoresistance in platinum on yttrium iron garnet: dependence on platinum thickness and in-plane/out-of-plane magnetization. *Phys. Rev. B* **87**, 184421 (2013).
- Kajiwara, Y. *et al.* Transmission of electrical signals by spin-wave interconversion in a magnetic insulator. *Nature* **464**, 262–267 (2010).
- Hamadeh, A. *et al.* Full control of the spin-wave damping in a magnetic insulator using spin-orbit torque. *Phys. Rev. Lett.* **113**, 197203 (2014).
- Chumak, A. V., Vasyuchka, V. I. I., Serga, A. A. A. & Hillebrands, B. Magnon spintronics. *Nat. Phys.* **11**, 453–461 (2015).
- Kubota, M. *et al.* Stress-induced perpendicular magnetization in epitaxial iron garnet thin films. *Appl. Phys. Exp.* **5**, 103002 (2012).
- Paoletti, A. *Physics of Magnetic Garnets* (North-Holland Publishing Company, 1978).
- Saitoh, E., Ueda, M., Miyajima, H. & Tatara, G. Conversion of spin current into charge current at room temperature: inverse spin-Hall effect. *Appl. Phys. Lett.* **88**, 182509 (2006).
- Meyer, S. *et al.* Anomalous Hall effect in YIG vertical bar Pt bilayers. *Appl. Phys. Lett.* **106**, 132402 (2015).
- Chen, Y. T. *et al.* Theory of spin Hall magnetoresistance. *Phys. Rev. B* **87**, 144411 (2013).
- Liu, L. Q., Moriyama, T., Ralph, D. C. & Buhrman, R. A. Spin-torque ferromagnetic resonance induced by the spin Hall effect. *Phys. Rev. Lett.* **106**, 36601 (2011).
- Kim, J. *et al.* Layer thickness dependence of the current-induced effective field vector in Ta vertical bar CoFeB vertical bar MgO. *Nat. Mater.* **12**, 240–245 (2013).
- Schreier, M. *et al.* Current heating induced spin Seebeck effect. *Appl. Phys. Lett.* **103**, 242404 (2013).
- Liu, L. Q., Lee, O. J., Gudmundsen, T. J., Ralph, D. C. & Buhrman, R. A. Current-induced switching of perpendicularly magnetized magnetic layers using spin torque from the spin Hall effect. *Phys. Rev. Lett.* **109**, 96602 (2012).
- Ibrahim, I., Schweigert, V. & Peeters, F. Diffusive transport in a Hall junction with a microinhomogeneous magnetic field. *Phys. Rev. B* **57**, 15416–15427 (1998).
- Avci, C. O. *et al.* Fieldlike and antidamping spin-orbit torques in as-grown and annealed Ta/CoFeB/MgO layers. *Phys. Rev. B* **89**, 214419 (2014).
- Lee, O. J. *et al.* Central role of domain wall depinning for perpendicular magnetization switching driven by spin torque from the spin Hall effect. *Phys. Rev. B* **89**, 024418 (2013).

## Acknowledgements

The authors would like to acknowledge support from C-SPIN, one of the six SRC STARnet Centers, sponsored by MARCO and DARPA. A.Q. acknowledges funding from the Deutsche Forschungsgemeinschaft (DFG, German Research Foundation) and from the Max-Planck-Institute of Microstructure Physics. C.O.A. and C.-F.P. thank K. Ueda and A. J. Tan for fruitful discussions.

## Author contributions

G.S.D.B. and C.A.R. proposed and supervised the study. C.O.A., M.M., C.-F.P. and G.S.D.B. designed the transport experiments. A.Q., A.S.T. and M.C.O. fabricated the TmIG samples. A.Q. performed structural and magnetic analysis. M.M. carried out photolithography processing. C.O.A., M.M. and A.Q. carried out transport measurements. M.M. and L.C. designed and established the electrical measurement equipment.

## Additional information

Supplementary information is available in the [online version of the paper](#). Reprints and permissions information is available online at [www.nature.com/reprints](http://www.nature.com/reprints). Correspondence and requests for materials should be addressed to C.A.R. or G.S.D.B.

## Competing financial interests

The authors declare no competing financial interests.

## Methods

**Material growth.** A stoichiometric TmIG target was fabricated using high-purity powders of the respective binary oxides, which were sintered and cold-pressed into a one-inch diameter target. The material was deposited onto 1 cm-by-1 cm GGG(111) substrates via PLD at a laser wavelength of 248 nm, a fluence of  $\sim 1.5 \text{ J cm}^{-2}$ , and a target-to-substrate distance of 5 cm. During deposition, the substrate temperature was 810 °C and the oxygen pressure was 200 mtorr. No post-deposition annealing process was performed, but the cooling step to room temperature at 200 mtorr oxygen pressure occurred at  $-5 \text{ °C min}^{-1}$ .

**Device fabrication.** After the deposition of the TmIG(8 nm) thin film via PLD, a 5-nm-thick layer of the spin Hall metal Pt was deposited by sputtering. The base pressure was  $9 \times 10^{-7}$  torr, and the deposition rate was  $1.5 \text{ nm min}^{-1}$ . Hall crosses with lateral dimensions of  $7 \mu\text{m} \times 6 \mu\text{m}$  were patterned via a top-down ion milling process after using a standard photolithography method to define the mesa structures. Ta(4 nm)/Au(100 nm) were deposited as contact pads for electrical measurements.

**Magnetic characterization.** In-plane and out-of-plane hysteresis loops were measured using VSM, and the out-of-plane loop shape was verified using

a polar MOKE magnetometer. A paramagnetic background from the substrate was subtracted from the VSM data shown in Fig. 1b. The MFM measurements were conducted within a scan area of  $10 \mu\text{m}^2$  using a magnetic Co/Cr-coated antimony-doped Si tip at a lift height of 20 nm.

**Electrical measurements.** Hall effect measurements reported in Fig. 2 were performed by injecting an a.c. voltage of  $V_{r.m.s.} = 0.5 \text{ V}$  with frequency  $\omega/2\pi = 3,678 \text{ Hz}$ , giving rise to a current of amplitude  $I_{r.m.s.} = 1.5 \text{ mA}$ , using a standard lock-in amplifier. A typical device resistance was  $R_{\text{device}} \approx 300 \Omega$ , to which a capacitor from a bias-T ( $1 \mu\text{F}$ ) and a resistor ( $50 \Omega$ ) were connected in series. The measured a.c. Hall voltage was averaged over several scans and was converted to a Hall resistance using  $R_{\text{H}} = (V_{\omega}/I)$ . To generate measurable torques and perform the harmonic measurements shown in Fig. 3, we increased the voltage to  $V_{r.m.s.} = 3 \text{ V}$  and recorded the second-harmonic Hall voltage. Each curve shown in Fig. 3b,c was averaged over 200 loops with a field sweep rate of 0.4 Hz. To perform the switching measurements reported in Fig. 4 we have used a bias-T ( $1 \mu\text{F}$ – $1.05 \text{ k}\Omega$ ) to decouple the output from the pulse generator and the lock-in amplifier. Pulses were generated by amplifying a digital-to-analog converter output with a Crown DC150 audio amplifier.